

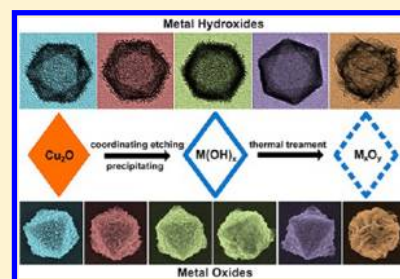
Pearson's Principle Inspired Generalized Strategy for the Fabrication of Metal Hydroxide and Oxide Nanocages

Jianwei Nai, Yu Tian, Xin Guan, and Lin Guo*

School of Chemistry and Environment, Beihang University, Beijing 100191, People's Republic of China

S Supporting Information

ABSTRACT: Designing a general route for rational synthesis of a series or families of nanomaterials for emerging applications has become more and more fascinating and vital in the view of nanoscience and nanotechnology. Herein, we explore a general strategy for fabricating uniform nanocages of metal hydroxides (MHs) and metal oxides (MOs). A template-assisted route inspired by Pearson's hard and soft acid–base (HSAB) principle was employed for synthesizing MH nanocages via meticulous selection of the coordinating etchant as well as optimization of the reaction conditions. The concept of “coordinating etching” is successfully achieved in this work. This unique route shows potential in designing well-defined and high-quality MH nanocages with varying components, shell thicknesses, shapes, and sizes at room temperature. Consequently, porous MO nanocages can be obtained readily just through appropriate thermal treatment of the respective MH nanocages. The overall strategy present in this work extends the application of the HSAB principle in nanoscience and offers a unique clue for rational fabrication of hollow (porous) and/or amorphous structures on the nanoscale, where these nanocages may present promising potential for various applications.



INTRODUCTION

“Chimie douce” (also known as soft chemistry) based strategies allow, through a deep knowledge of materials chemistry and processing, the birth of the molecular engineering of nanomaterials and the rational design of specific nanostructures.¹ Basically, rational design implies two steps: the first is to identify the right kind of architecture and probable chemical composition that would give rise to the desired property, and the next step is to find an appropriate procedure to synthesize the material. Particularly, realizing shape-controlled fabrication, such as photomediated,² stepwise evolution,³ seed-mediated,^{4–6} template-assisted,^{7,8} etc., is very important for the development of nanomaterials, since their properties are usually structure-dependent. Recently, designing a general route for rational synthesis of a series or families of nanomaterials for emerging applications^{9–19} has become more and more fascinating and vital in the view of nanoscience and nanotechnology, because this would provide not only a great deal of opportunities for studying the relation between the structures and properties of the nanomaterials obtained by a similar approach²⁰ but also a clue to design new types of nanomaterials with desired properties through referencing a given methodology. Nevertheless, the general routes reported so far have mainly focused on synthesizing solid nanomaterials or cagelike/hollow nanostructures that are limited to noble metals. The design of a simple method with broad applicability for the synthesis of high-quality nanocages of metal compounds, e.g. metal hydroxides and oxides, still remains as a significant challenge.

Owing to their low density, excellent loading capacity, high permeability, and specific surface area, cagelike/hollow nanostructures have attracted growing interest in recent years

and deserve more attention in controllable preparation because of their wide application.^{21–23} Specifically, anisotropic nanocages with nonspherical shapes and regular interiors are of particular interest for their unique advantages.^{24–26} For instance, anisotropic cages are beneficial in biomedical applications,²⁵ targeted drug delivery,²⁶ and energy storage.²⁷ Their anisotropic features even offer them the possibility to be essential building blocks of complex hierarchical architectures with multiple functionalities.²⁸ In addition, these anisotropic cages also show better performance in applications in comparison with solid materials. Xia et al. demonstrated that the good intrinsic electrical connection across the entire surface of Au cubic nanocages makes them much better catalysts than small Au solid nanoparticles for a redox reaction.²⁹ In comparison with solid Co₃O₄, cagelike Co₃O₄ nanostructures were found to have lower initial irreversible loss, higher reversible capacity, and excellent capacity retention in a test of electrochemical lithium storage, which was attributed to their hollow polyhedral structures.³⁰ Even when the same feature of a hollow interior is preserved, nonspherical cages still have advantages over spherical cages. For example, hollow polyhedral nanomaterials manifest greatly enhanced lithium storage properties in comparison to porous/hollow spheres, in terms of both storage capacity and cycling stability.^{31,32} Qian et al. also found that cubic microcages can be a better adsorbent than spherical or ellipsoid-like microcages in water treatment for removing phenol.³³ Though the applications of these anisotropic nanocages are promising, the fabrication is often

Received: March 18, 2013

Published: May 31, 2013

difficult to achieve through conventional approaches, such as inside-out Ostwald ripening and self-assembly.^{34–37} Template-assisted routes can be straightforward in concept for the synthesis of nanocages and the possible creation of non-spherical nanostructures.³⁸ However, even with templating strategies, there have not been many good examples of anisotropic nanocages reported, possibly due to additional technological difficulties such as (i) mastery of the reaction kinetics balance between the growth of a shell with desirable materials and the synchronous removal of the sacrificial templates, (ii) formation of a uniform coating around high-curvature surfaces of the nonspherical templates, (iii) preservation of the shape with high residual stresses, and (iv) the lack of proper and easily obtained nonspherical templates. In recent years, some novel template-assisted approaches based on different principles such as the Kirkendall effect, galvanic replacement, and chemical etching have been developed for the efficient preparation of various cagelike/hollow nanostructures.^{10,16,39–42} It should be mentioned that Wang et al. recently reported an interesting synthesis of SnO₂ nanoboxes by “coordinating etching” Cu₂O templates using a Cl[−] ligand.⁴³ However, a similar experiment carried out by us (Experiment S1 and Figure S1, Supporting Information) reveals that it might be acid (H⁺) etching rather than coordinating (Cl[−]) etching dominating the reaction process in their work. Therefore, no matter the methods adopted above, the fundamental principle for the template removal is self-diffusion or acidic or oxidative/redox etching.

Herein, we explore a general strategy for fabricating uniform nanocages of metal hydroxides (MHs) by templating against Cu₂O nanocrystals at room temperature and then obtaining metal oxide (MO) porous nanocages by simple thermal treatment of the as-prepared MHs. Cu₂O nanocrystals are employed as sacrificial templates because they (i) present diversity in crystal morphology, especially nonspherical shapes such as cubes, octahedra, and other highly symmetrical structures,^{44–48} (ii) would provide favorable solution conditions for the precipitation of desired shell materials (see the equations in the following discussion), and (iii) can be obtained via a facile route. The key of this unique strategy lies in the fabrication of MHs, which is inspired by Pearson’s hard and soft acid–base (HSAB) principle.⁴⁹ This classic coordination chemistry principle has not been taken full advantage of in materials synthesis at the nanoscale,^{19,50,51} though it has already been applied in the film processing of the early photographic industry, where silver bromide (Ag⁺ is a soft acid), a typical component of photographic emulsions, dissolves easily upon treatment with aqueous thiosulfate (S₂O₃^{2−} is a soft base).^{52,53} The concept of “coordinating etching” is successfully achieved in this work. A “coordinating etching and precipitating” (CEP) route is implemented by deliberately mastering the balance of the precipitating rate of metal hydroxides and the synchronous coordinating etching rate toward the sacrificial template. MHs and MOs with several transition-metal elements (M = Mn, Fe, Co, Ni, Zn) have been chosen to demonstrate the effectiveness of this method, in view of the limited success in synthesizing nanocages of these materials, and their significant applications in advanced memory, optical, and electronic devices.^{54–57}

EXPERIMENTAL SECTION

Preparation of Solid Cu₂O Crystals. The synthesis follows our previous report with minor modification.^{44,45} The cubic, octahedral,

and spherical nanostructures of Cu₂O samples are shown in Figure S2 in the Supporting Information.

Preparation of M(OH)_x (M = Mn, Fe, Co, Ni, Zn, Pb) Nanocages. In a typical procedure, a certain amount of Cu₂O templates and MCl₂·yH₂O were added to 10 mL of the ethanol/water mixed solvent in the presence of PVP (*M_w* = 30,000). After the mixture was stirred for 10 min, a certain amount of Na₂S₂O₃ aqueous solution was added dropwise. Then the reaction was carried out at room temperature for some time until the suspension solution changed from red to the expected color. Eventually, M(OH)_x nanocages were fabricated. For details of the reaction conditions see Table S1 in the Supporting Information.

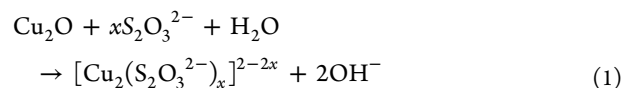
Preparation of M_xO_y (M = Mn, Fe, Co, Ni, Zn, Pb) Nanocages. In a typical procedure, the as-prepared M(OH)_x samples were treated with calcination under an argon or air atmosphere at different temperatures for a certain time. The heating rate was kept at 1 °C min^{−1} for each sample. After thermal treatment, M_xO_y nanocages were obtained. For details of the calcination conditions see Table S2 in the Supporting Information.

Characterization. The structures of the as-prepared products were characterized by X-ray powder diffraction (XRD) using a Shimadzu X-lab6000 X-ray diffractometer with Cu Kα radiation (λ = 1.5416 Å). X-ray photon spectroscopy (XPS) was recorded with a Thermo Scientific ESCALAB 250 Xi XPS system, where the analysis chamber was 1.5 × 10^{−9} mbar and the size of the X-ray spot was 500 μm. All of the spectra were referenced to the C 1s binding energy (BE) of 284.8 eV. Spectra were analyzed using CasaXPS software (version 2.3.14). The morphologies and element composition of the synthesized samples were prepared on Si substrates and studied by a JEOL JSM-7500F cold-field emission scanning electron microscope (CFESEM) and its affiliated energy dispersive X-ray diffraction spectroscopy (EDS); transmission electron microscopy (TEM) investigations were carried out with a JEOL JEM-2100 microscope.

RESULTS AND DISCUSSION

Strategy for the MH and MO Nanocages Fabrication.

On the basis of the HSAB principle, on one hand soft Lewis bases can form stable complexes with soft acids; hard bases, on the other hand, prefer hard acids. Hence, selecting a soft base ligand (S₂O₃^{2−}, CN[−], SCN[−], etc.) as the coordinating etchant should be more appropriate and efficient than a hard base (Cl[−], NH₃, etc.) due to the soft acid feature of Cu⁺ within the Cu₂O templates. Nevertheless, not all the soft bases can be competent in our synthetic strategy. For example, CN[−] is a C-coordinated ligand which has an empty π* orbital. Thus, it can accept an electron pair from the t_{2g} orbit of the central metal ion to form π back-donation, which would significantly enhance the chemical affinity of CN[−] with the transition-metal ions. This would restrain the generation of MHs even though the Cu₂O can be coordinating etched. SCN[−] should not be considered as the etchant either, because it could induce the impurity of the product, since CuSCN is insoluble. More information on the acid–base binding affinity could be obtained from a comparison of the stability constants of diverse coordination compounds (Table S3, Supporting Information). The solubility product constants of various MHs that are proposed to precipitate are also shown in Table S4 (Supporting Information). In the case of this work, the synthetic strategy of MHs is designed by employing Na₂S₂O₃ as the coordinating etchant. The formation process is illustrated as steps 1 and 2 in Figure 1, and the general chemical route could be described as



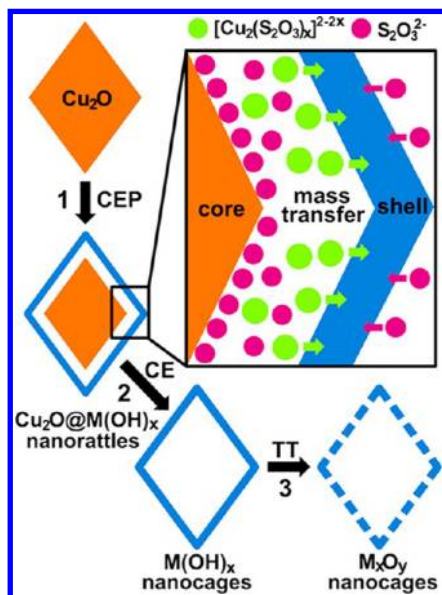
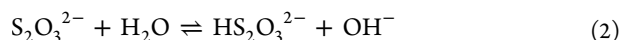


Figure 1. Schematic illustration of the fabrication of $\text{M}(\text{OH})_x$ ($\text{M} = \text{Mn, Fe, Co, Ni, Zn}$) nanocages by synchronous coordinating etching of Cu_2O nanocrystals and the fabrication of M_xO_y by thermal treating of relevant $\text{M}(\text{OH})_x$. Abbreviations used: CEP, coordinating etching and precipitating; CE, coordinating etching; TT, thermal treatment.

During this process, $\text{S}_2\text{O}_3^{2-}$ species introduced to the solution system can play versatile roles: (i) coordinating etching of Cu_2O (eq 1) occurs by forming a soluble $[\text{Cu}_2(\text{S}_2\text{O}_3)_x]^{2-2x}$ complex, since the soft–soft interaction of $\text{Cu}^+ - \text{S}_2\text{O}_3^{2-}$ is much stronger than the soft–hard interaction of $\text{Cu}^+ - \text{O}^{2-}$ within Cu_2O ; (ii) other transition-metal ions (M^{2+}) are left nearly free in the solution due to the unstable binding of borderline acid–soft base ($\text{M}^{2+} - \text{S}_2\text{O}_3^{2-}$); (iii) along with the OH^- released from the etching of Cu_2O (eq 1), those OH^- originating from hydrolysis of some $\text{S}_2\text{O}_3^{2-}$ (eq 2) can also facilitate the formation of $\text{M}(\text{OH})_2$ (eq 3). Specifically, the pH of the $\text{Na}_2\text{S}_2\text{O}_3$ solution used in the typical procedure is slightly alkaline (9.35 for the solution with 1 M $\text{Na}_2\text{S}_2\text{O}_3$ or 8.50 for that with 0.2 M $\text{Na}_2\text{S}_2\text{O}_3$). Nevertheless, the pH of the reaction systems for fabricating different MHs can all reach over 10 (Table S1, Supporting Information), since much more OH^- would be released when $\text{S}_2\text{O}_3^{2-}$ etches Cu_2O (eq 1). Hence, when the etching process occurs, $\text{M}(\text{OH})_2$ starts precipitating synchronously and the shell structure prefers to form around the etching interface where the local concentration of OH^- is the highest. This process is defined as “coordinating etching and precipitating” (CEP) and is demonstrated as step 1 in Figure 1. Herein these two synchronous chemical reaction guarantee that the exterior of $\text{M}(\text{OH})_2$ shell perfectly imitates the geometrics of Cu_2O templates. The shell structure can be reserved in the following coordinating etching (CE) procedure (step 2), even though in some cases (Mn and Fe) the $\text{M}(\text{OH})_2$ might transform to $\text{M}(\text{OH})_x$ due to the oxidation (see the following discussion of XPS results). It should be noted that, on one hand, the thickness of the MH shell would increase as the reaction proceeds until the concentration of metal ions decreases to a value that cannot meet the request of

precipitation (occurs only in step 1). On the other hand, continuous dissolution of Cu_2O can occur even in closed shells, proving that species such as $\text{S}_2\text{O}_3^{2-}$ and the $[\text{Cu}_2(\text{S}_2\text{O}_3)_x]^{2-2x}$ complex can freely transport across the shells through interparticle interstitials and driven by the as-buildup concentration gradient during the etching process (occurs in both steps 1 and 2). The evolution of the hollow interior (Figure S3, Supporting Information) monitored by sampling at intervals and characterizing with TEM also supports the mechanism of steps 1 (CEP) and 2 (CE). The strong affinity between the etchant and the template makes fabrication at low temperature possible. In addition, the reaction is completed rapidly without addition of any extra oxidizing or acid agents. In this regard, the “coordinating etching” mechanism involved in the present system differs in concept from the traditional hollow-engendered mechanism, such as self-diffusion or acidic or oxidative/redox etching, toward the sacrificial templates. In a further procedure, MO porous nanocages can be readily obtained by the common thermal treatment of the as-prepared MHs, illustrated as step 3 in Figure 1.

Component and Crystallographic Structure Analysis of the MH Nanocages. The as-synthesized MHs samples, including manganese hydroxide, iron hydroxide, cobalt hydroxide, nickel hydroxide, and zinc hydroxide, were first evaluated by XPS. The XPS spectra of $\text{M } 2p_{3/2}$ and $\text{O } 1s$ of these five samples are compared in Figure 2. The respective curve-fitted results are given in Table 1.

Analysis of the XPS Data of Manganese Hydroxide. According to the systematic study of XPS spectra of transition-metal hydroxides reported by Biesinger,⁵⁸ the main peak 2 at 641.8 eV in the $\text{Mn } 2p_{3/2}$ spectrum (Figure 2a) should be assigned to Mn^{3+} , whose other peak was fitted at 643.1 eV (peak 3); peak 1 at 640.6 eV could be assigned to Mn^{2+} . Therefore, it can be inferred that two valence states of manganese ions coexist in the sample, which can also be supported by analyzing the spectrum of $\text{O } 1s$. In Figure 2b, an obvious fitted peak 1 at 529.4 eV should result from the lattice oxygen, “ions O^{2-} ”,⁵⁹ which cannot be obviously observed from the $\text{O } 1s$ spectra of nickel hydroxide (Figure 2f), cobalt hydroxide (Figure 2h), or zinc hydroxide (Figure 2j). The enhancement of this peak should be attributed to more lattice oxygen species binding the central metal ions when some of these metal ions transfer to a higher valence state (Mn^{2+} oxidizes to Mn^{3+}). This observation is in good agreement with the result found in the $\text{Mn } 2p_{3/2}$ spectrum. Peak 2 (530.5 eV) and peak 3 (530.9 eV) can be assigned to two types of oxygen species integrated in the material as “ions OH^- ”, associating with Mn^{2+} and Mn^{3+} , respectively. Peak 4 at 531.5 eV can be assigned to the “ions O^- ”, which could allow compensation for some deficiencies in the subsurface of the material.⁶⁰ To sum up, the component of this sample might be a composite of $\text{Mn}(\text{OH})_2$ and $\text{MnO}(\text{OH})$, where $\text{MnO}(\text{OH})$ could be generated from the oxidation of $\text{Mn}(\text{OH})_2$ (the common oxidation result of $\text{Mn}(\text{OH})_2$ is $\text{MnO}(\text{OH})$ but not $\text{Mn}(\text{OH})_3$). This can be also supported by the observation of the dark brown color, the characteristic color of $\text{MnO}(\text{OH})$, of the sample solution (see the inset of Figure 3a₁).

Analysis of the XPS Data of Iron Hydroxide. According to ref 58, the main peak at 711.4 eV and all the other fitted peaks in the $\text{Fe } 2p_{3/2}$ spectrum (Figure 2c) should be assigned to Fe^{3+} in $\text{Fe}(\text{OH})_3$. In Figure 2d, the enhanced peak 1 at 529.4 eV, similar to that in Figure 2b, also indicates the existence of the high valence state of the iron ion (Fe^{3+}). Peak 2 at 530.9 eV can

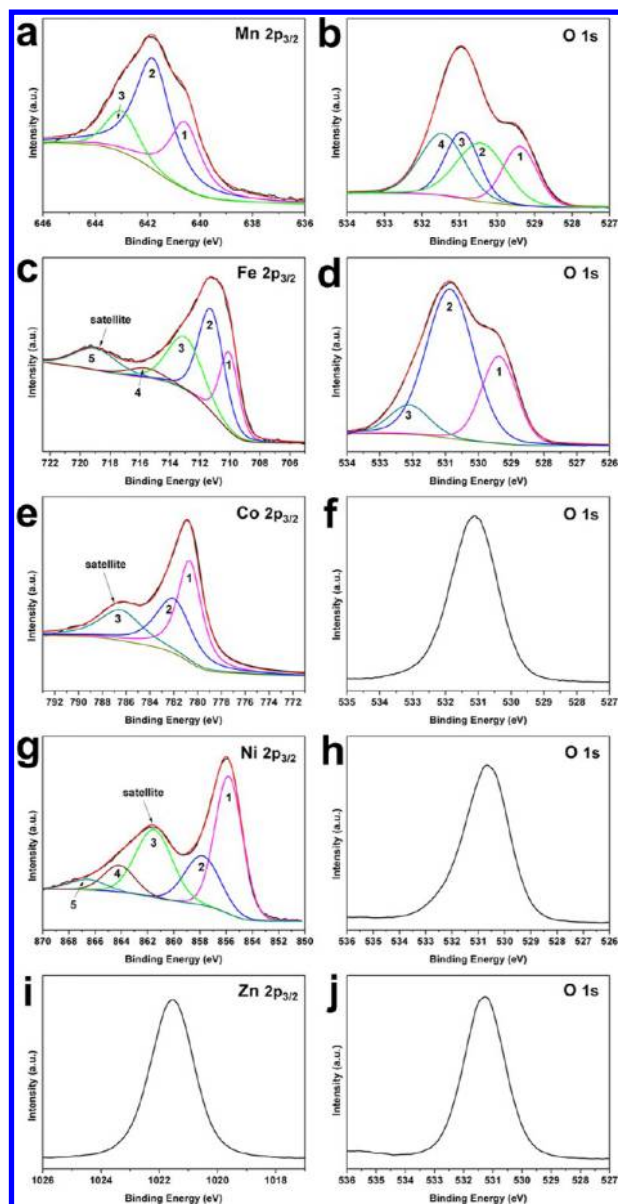


Figure 2. XPS spectra of the as-prepared samples of (a, b) manganese hydroxide, (c, d) iron hydroxide, (e, f) cobalt hydroxide, (g, h) nickel hydroxide, and (i, j) zinc hydroxide.

be assigned to the “ions OH^- ”, and peak 3 at 532.1 eV should be associated with weakly adsorbed oxygen species.⁶⁰ To sum up, the component of this sample should be $\text{Fe}(\text{OH})_3$, where the preformed $\text{Fe}(\text{OH})_2$ might be all oxidized to $\text{Fe}(\text{OH})_3$. This can be also supported by the observation of the russet color, the characteristic color of $\text{Fe}(\text{OH})_3$, of the sample solution (see the inset of Figure 3b₁).

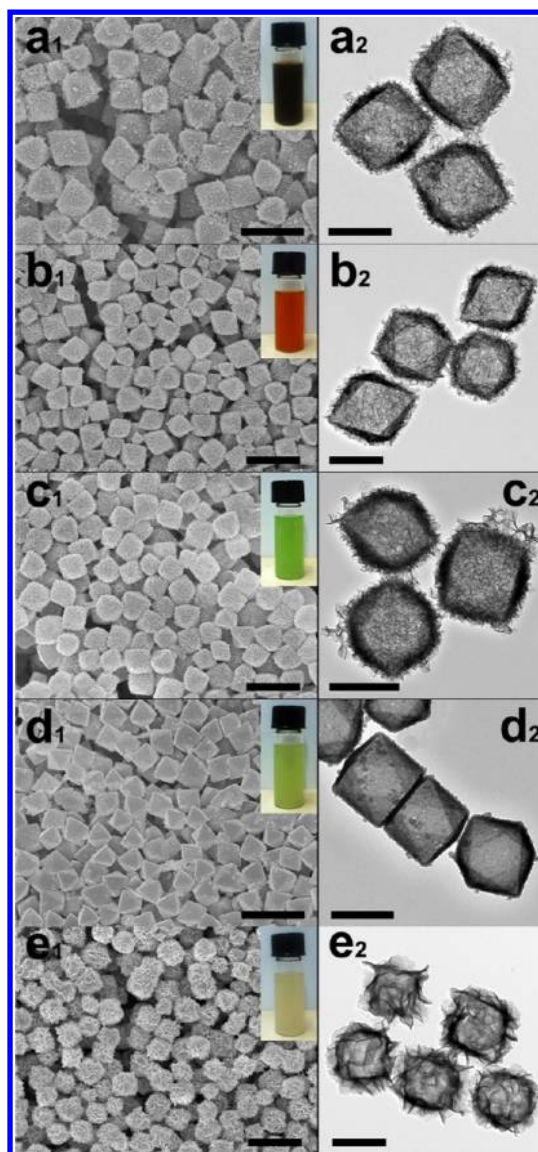


Figure 3. Overview SEM images and TEM images of the (a) manganese, (b) iron, (c) cobalt, (d) nickel, and (e) zinc hydroxide nanocages. Insets of x_1 ($x = a-e$) are digital photos and show the colors of the sample solutions. The scale bars in parts x_1 and x_2 are 1 μm and 500 nm, respectively.

Analysis of the XPS Data of Cobalt Hydroxide. According to ref 58, the main peak at 780.7 eV and all the other fitted peaks in the Co $2p_{3/2}$ spectrum (Figure 2e) should be assigned to Co^{2+} in $\text{Co}(\text{OH})_2$. In Figure 2f, the peak at 531.0 eV can be assigned to the “ions OH^- ”.⁶⁰ To sum up, the component of this sample should be $\text{Co}(\text{OH})_2$. This can be also supported by the observation of the jade green color, one of the characteristic

Table 1. Curve-Fitted XPS Binding Energies of the Five Metal Hydroxide Samples

peak	M $2p_{3/2}$ (eV)					O 1s (eV)				
	Mn	Fe	Co	Ni	Zn	Mn	Fe	Co	Ni	Zn
1	640.6	710.1	780.7	855.8	1021.5	529.4	529.4	531.0	530.7	531.1
2	631.8	711.4	782.2	857.9		530.5	530.9			
3	643.1	713.2	786.6	861.6		530.9	532.1			
4		715.9		864.2		531.5				
5		719.2		866.7						

colors of $\text{Co}(\text{OH})_2$, of the sample solution (see the inset of Figure 3c₁).

Analysis of the XPS Data of Nickel Hydroxide. According to ref 58, the main peak at 855.8 eV and all the other fitted peaks in the Ni 2p_{3/2} spectrum (Figure 2g) should be assigned to Ni²⁺ in $\text{Ni}(\text{OH})_2$. In Figure 2h, the peak at 530.7 eV can be assigned to the “ions OH⁻”.⁶⁰ To sum up, the component of this sample should be $\text{Ni}(\text{OH})_2$. This can be also supported by the observation of the light green color, the characteristic color of $\text{Ni}(\text{OH})_2$, of the sample solution (see the inset of Figure 3d₁).

Analysis of the XPS Data of Zinc Hydroxide. The peak at 1021.5 eV in the Zn 2p_{3/2} spectrum (Figure 2i) should be assigned to Zn²⁺ in $\text{Zn}(\text{OH})_2$.⁶¹ In Figure 2j, the peak at 531.1 eV can be assigned to the “ions OH⁻”.⁶⁰ To sum up, the component of this sample should be $\text{Zn}(\text{OH})_2$. This can be also supported by the observation of the white color, the characteristic color of $\text{Zn}(\text{OH})_2$, of the sample solution (see the inset of Figure 3e₁).

To summarize the XPS results, the components of these five different samples should be $\text{Mn}(\text{OH})_2/\text{MnO}(\text{OH})$, $\text{Fe}(\text{OH})_3$, $\text{Co}(\text{OH})_2$, $\text{Ni}(\text{OH})_2$, and $\text{Zn}(\text{OH})_2$, respectively. Though some contaminant elements, e.g. Na, Cu, and S, which might be derived from the adsorbed $\text{Na}_2\text{S}_2\text{O}_3$ etchant and $[\text{Cu}_2(\text{S}_2\text{O}_3)_x]^{2-2x}$ complex, can be also detected in the full range of XPS patterns, the relevant intensities of these elements are very weak (Figure S4, Supporting Information). This indicates the low proportion of the contaminant elements in each sample, which can be also proved by the investigation of EDS (Figure S5, Supporting Information). It should be mentioned that the oxidation of $\text{Mn}(\text{OH})_2$ and $\text{Fe}(\text{OH})_2$ can still occur in the presence of a common reductant, thiosulfate. The reason is as follows: the thiosulfate could be oxidized to sulfate (SO_4^{2-}), a high oxidation state, in the present of strong oxidant (e.g., Cl_2 or MnO_4^-) or under the strongly alkaline (1 M NaOH) conditions with heating.⁶² However, none of these strongly oxidizing conditions can be found in our reaction system. Otherwise, another common oxidation product of thiosulfate is tetrathionate ($\text{S}_4\text{O}_6^{2-}$), a relatively low oxidation state.⁶² Since the standard reduction potentials (vs SHE) of the $\text{Fe}(\text{OH})_3/\text{Fe}(\text{OH})_2$ pair, $\text{MnO}(\text{OH})/\text{Mn}(\text{OH})_2$ pair, O_2/OH^- pair, and $\text{S}_4\text{O}_6^{2-}/\text{S}_2\text{O}_3^{2-}$ pair are -0.56, 0.10, 0.40, and 0.08 V, respectively, the preformed $\text{Fe}(\text{OH})_2$ or $\text{Mn}(\text{OH})_2$ could be easily oxidized to $\text{Fe}(\text{OH})_3$ or $\text{MnO}(\text{OH})$ by oxygen in the open reaction system in our work and would not be reduced by thiosulfate after the oxidation. XRD patterns (Figure S6, Supporting Information) reveal the amorphous feature of all five samples as expected, since the synthesis is carried out at room temperature and completed rapidly.

Morphology Characterization of MH and MO Nanocages. Overview SEM images and low-magnification TEM images in Figure 3 show that each sample consists of uniform and high-quality nanocages without impure particles or aggregates. The insets of Figure 3 show the typical color of each sample, which support the component analysis above. High-magnification SEM and TEM images of the typical MH nanocages are shown in Figure 4 to provide a clear view of these architectures. Figure 4x₁ (x = a–e) reveal the cage-like MHs have an octahedral structure with an edge length of ~500 nm, which inherit the geometrics and dimensions of the Cu_2O template well. It can be clearly observed from Figure 4x₂ that small particles constitute the shell structure. In addition, these small particles are active and therefore easily aggregate to form varying degrees of wormlike secondary structures on the surface

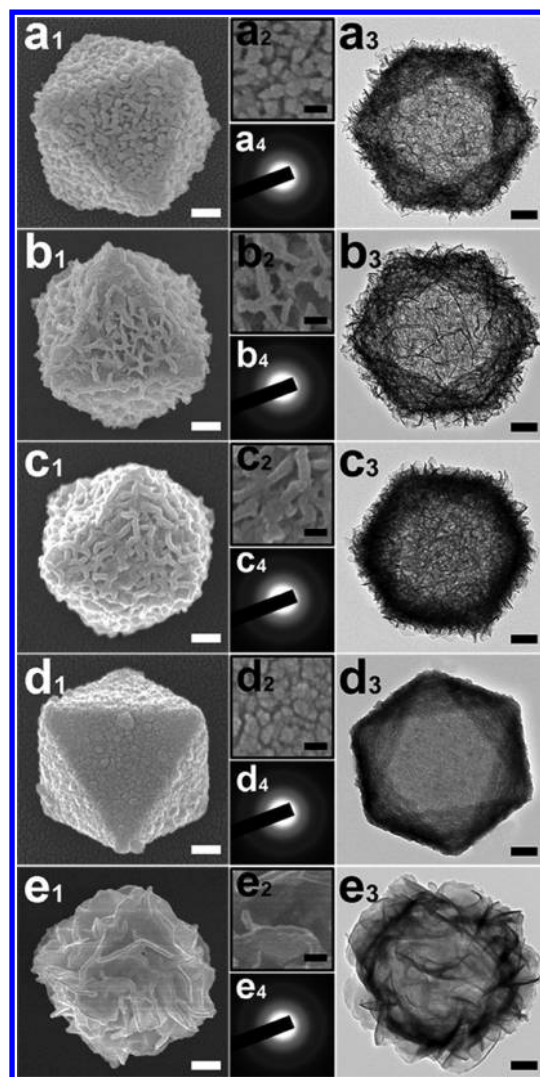


Figure 4. SEM, TEM, and SAED images of the (a) manganese, (b) iron, (c) cobalt, (d) nickel, and (e) zinc hydroxide nanocages. Parts x₁ (x = a–e) and x₃ show a typical metal hydroxide cage image by SEM and TEM, respectively; part x₂ shows high-magnification images of the surface of the cage in part x₁; part x₄ is the SAED pattern obtained from the whole cage in part x₃. The scale bars in parts x₁, x₂, and x₃ are 100, 20, and 100 nm, respectively.

of the cages to reduce the system energy. It should be noted that the morphology of the zinc hydroxide nanocages appears to be slightly different from that of the other metal hydroxides. Their shell appears to be more sheetlike and loosely packed. This is because the smallest solubility product constant (Table S4, Supporting Information) and relatively high pH of the reaction system (Table S1, Supporting Information) can induce a faster nucleation of zinc hydroxide into small particles which then aggregate in a greater degree. Therefore, the secondary structures of zinc hydroxide seem more sheetlike, while those of other materials, e.g. cobalt hydroxide, seem wormlike. These sheetlike structures cause the shell to be loosely packed, but the shell framework can still maintain the basic octahedral architecture.

The hollow interior and architectural construction of as-prepared $\text{M}(\text{OH})_x$ nanocages have been further studied by TEM images, as displayed in Figure 4x₃. The inner cavity is clearly revealed by the contrast between the shells and hollow

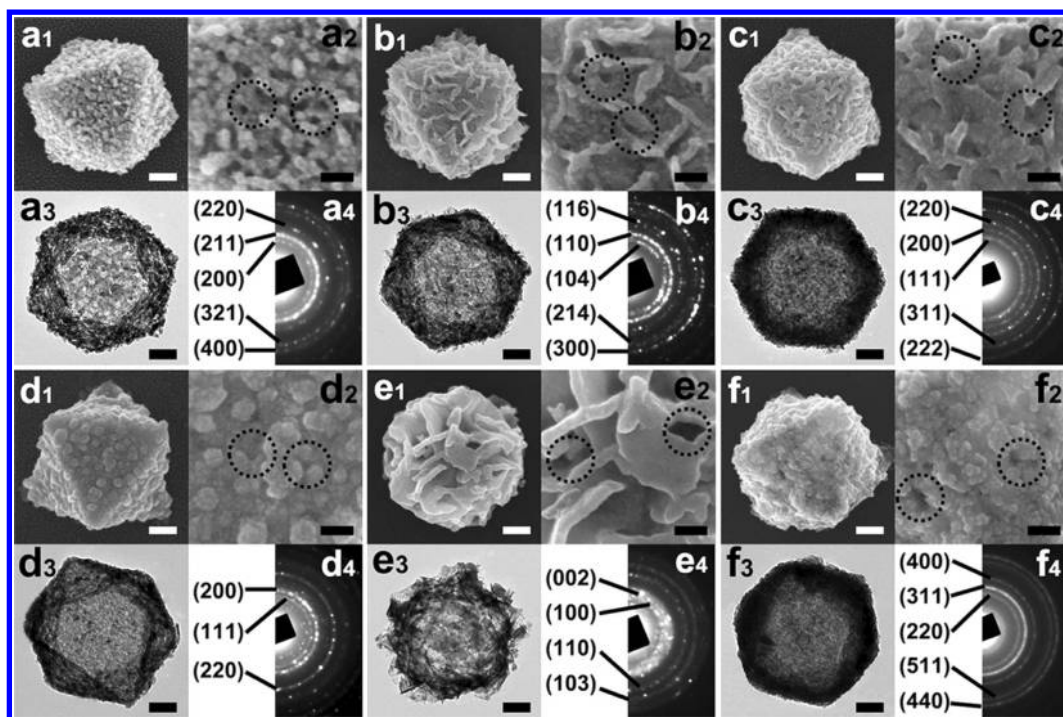


Figure 5. SEM, TEM, and SAED images of the (a) Mn_3O_4 , (b) Fe_2O_3 , (c) CoO , (d) NiO , (e) ZnO , and (f) Co_3O_4 nanocages. Parts x_1 ($x = \text{a–f}$) and x_3 show a typical metal oxide cage image by SEM and TEM, respectively; part x_2 shows high-resolution images of the surface of the cage in part x_1 , with porous structures pointed out in circles; part x_4 is the SAED pattern obtained from the whole cage in part x_3 . The scale bars in parts x_1 , x_2 , and x_3 are 100, 40, and 100 nm, respectively.

interiors. The highly symmetric octahedral shell framework can be observed more distinctly from these perspective views. The shell of the nanocages is as thin as ~ 40 nm. One would expect the nonspherical template should lead to nonuniform shell thickness because of enhanced reactivity at the corners and edges of the template, but we did not observe this effect. This result might be attributed to the equally high reactivity of the eight faces of the Cu_2O octahedron, since the coordination unsaturated “Cu” species on these faces³⁷ is also active to interact with $\text{S}_2\text{O}_3^{2-}$. No structural deformation such as warping or collapse occurs, though the reaction proceeds quite quickly. The selected area electron diffraction (SAED) patterns in Figure 4 x_4 also suggest the amorphous feature of these MH nanocages, consistent with the XRD result. Amorphous materials are well-known as containing numerous undercoordinated atoms or reactive sites at the surface, which would have a unique influence on the internal structures of the materials. Thus, the as-prepared amorphous MH nanocages may find interesting application in the field of electrochemistry^{63–66} and photochemistry.^{67,68}

After simple thermal treatment of the as-synthesized MHs samples, relevant MOs nanocages were readily obtained. XRD results (Figures S7a–S11a, Supporting Information) reveal that calcining the five hydroxide samples under an argon atmosphere can produce Mn_3O_4 , Fe_2O_3 , CoO , NiO , and ZnO , respectively. This result also supports our aforementioned component analysis of MH samples that there are two valence states (Mn^{2+} and Mn^{3+}) in the sample of manganese hydroxides, while there is only one state (Fe^{3+}) in the sample of iron hydroxides. Interestingly, another type of cobalt oxide, Co_3O_4 , can also be obtained when carrying out the calcination of cobalt hydroxides in the air (Figure S12a, Supporting Information). This is attributed to the fact that some Co^{2+} can

be oxidized to Co^{3+} under the oxygen-rich conditions. However, other types of MOs with further oxidation, e.g. Mn_2O_3 , cannot be obtained by a similar approach.

Overview SEM images and low-magnification TEM images (Figures S7b–S12b, Supporting Information) show that each sample consists of uniform nanocages without small particles even after calcination. High-magnification SEM and TEM images of the typical MO nanocages are shown in Figure 5. Figure 5 x_1 ($x = \text{a–f}$) reveals that the cage-like MOs still maintain the octahedral geometries and dimensions of the relevant MH nanocages. The octahedral shell structures can be observed more obviously from the TEM image in Figure 5 x_3 . Pores can be created on the shell of these MO nanocages (pointed out in circles in Figure 5 x_2), which are induced by the loss of constitutional water when hydroxides transform to oxides. Meanwhile, no obvious structural destruction such as collapse or deformation occurs after calcination, indicating that the present cage-like nanostructures are stable at the respective calcination temperatures. The SAED patterns in Figure 5 x_4 show the polycrystalline features of these MO nanocages. It should be mentioned that though the crystallinity of these MOs is not that good, from an observation of XRD and SAED results, this instead might be conducive to their applications in view of some recent reports.^{20,63–70} For instance, materials with the feature of an amorphous state, an extreme case of poor crystallinity, were found to have promising applications in the field of electrochemistry and photochemistry,^{63–68} poorly crystalline nanomaterials can also show better performance in electrochemical catalysis²⁰ and as capacitors.^{69,70} It is well-known that porous hollow materials can provide large surface areas for reaction, interfacial transport, or dispersion of active sites at different length scales of pores and shorten diffusion paths or reduce the diffusion effect. Hence, the as-obtained

porous MO nanocages may find a promising future in the applications of catalysis, sensors, energy conversion, and storage.^{71,72}

Discussion of the CEP Reaction System. From the above discussion, one can perceive that the fabrication of the MH nanocages, i.e. the CEP procedure, is the most fascinating and important part of this novel strategy. In the present system, precisely manipulating two synchronous processes, the precipitation of the shell materials and the coordinating etching of Cu_2O templates, is crucial for fabricating high-quality $\text{M}(\text{OH})_x$ nanocages. Taking $\text{Ni}(\text{OH})_2$ for example, if the strategy was carried out in the solvent system with only water, then excessive hydrolysis of $\text{S}_2\text{O}_3^{2-}$ (eq 2) would cause a high concentration of OH^- in the bulk solution. This would provide an opportunity for some Ni^{2+} to precipitate far from the etching interface and inevitably form abundant irregular particles, some of which might further induce severe collapse of nanocages by rapid mass transport across the shells (Figure S13a, Supporting Information). Meanwhile, the hydrolysis-induced decrease of the concentration of $\text{S}_2\text{O}_3^{2-}$ would lower the rate of coordinating etching of Cu_2O (eq 1), resulting in a prolonged reaction time. Therefore, a nonaqueous solvent such as ethanol should be introduced into the system to control the hydrolysis of $\text{S}_2\text{O}_3^{2-}$. However, too much ethanol would not be appropriate either. For example, in the solvent system with only ethanol, OH^- release is significantly inhibited due to the lack of water and decreased ionizability. Moreover, the poor solubility of $\text{Na}_2\text{S}_2\text{O}_3$ in ethanol lessens its coordinating etching ability toward Cu_2O . Thus, only a few $\text{Ni}(\text{OH})_2$ nanocages form (Figure S13b, Supporting Information). For fabricating nanocages with different components, the initial volumes of water and ethanol are not the same: i.e., 3 and 7 mL for manganese hydroxide, 10 and 0 mL for iron hydroxide, and 5 and 5 mL for cobalt, nickel, and zinc hydroxides. This difference can be attributed to the diversity of the solubility product constants of these MHs (Table S4, Supporting Information).

The concentration of the $\text{Na}_2\text{S}_2\text{O}_3$ added to the reaction system should also be considered. In the case of fabricating $\text{Ni}(\text{OH})_2$ nanocages, the concentration of $\text{Na}_2\text{S}_2\text{O}_3$ should be kept at 1 M. If the concentration of $\text{Na}_2\text{S}_2\text{O}_3$ was too high (e.g., 1.5 M), abundant irregular particles would appear in the sample, similar to the phenomenon of manipulating the reaction in the solvent system with only water (Figure S13a, Supporting Information). A relatively low concentration of $\text{Na}_2\text{S}_2\text{O}_3$ (e.g., 0.5 M) could reduce the concentration gradient of the etching procedure and thus the diffusion rate of $\text{S}_2\text{O}_3^{2-}$ would decrease consequently, which would significantly increase the reaction time. Therefore, an extremely high or low concentration would not maintain the balance between $\text{M}(\text{OH})_x$ formation rate and Cu_2O removal rate. Additionally, an alternative coordinating etchant with a soft base feature, $(\text{NH}_4)_2\text{S}_2\text{O}_3$ or $\text{CH}_4\text{N}_2\text{S}$, was also successfully applied in this reaction system. Uniform nanocages (e.g., $\text{Ni}(\text{OH})_2$) can also be readily synthesized (Figure S14, Supporting Information). Nevertheless, using either of these two etchants would prolong the reaction time compared with that for $\text{Na}_2\text{S}_2\text{O}_3$. This is because the neutral pH of these two etchant solutions would lead to a low concentration of OH^- ions in the reaction system and thus retard the precipitation of the MHs. Even after the reaction was complete, the pHs of the reaction systems using $(\text{NH}_4)_2\text{S}_2\text{O}_3$ and $\text{CH}_4\text{N}_2\text{S}$ can only reach 8.10 and 8.45, respectively, which are much lower than that for $\text{Na}_2\text{S}_2\text{O}_3$

(Table S1, Supporting Information). It is also found that introducing a surfactant such as polyvinyl pyrrolidone (PVP) to the synthetic system is indispensable in forming high-quality products. In the absence of PVP, $\text{Ni}(\text{OH})_2$ hollow nanostructures for instance, could still be produced, but not all the cage structures can be retained. Some irregular $\text{Ni}(\text{OH})_2$ particles also appeared (Figure S15, Supporting Information). In addition, PVP might also reduce the mobility of $\text{S}_2\text{O}_3^{2-}$ and thus slow down the etching reaction,⁷³ guaranteeing the production quality. Apart from the nonionic surfactant PVP, other common ionic surfactants, e.g. cetyltrimethylammonium bromide (CTAB) and sodium dodecyl sulfate (SDS), can also assist the fabrication of nanocages (Figure S16, Supporting Information), indicating a wide inclusivity of this system toward the types of surfactants. As a result, well-defined and high-quality $\text{M}(\text{OH})_x$ nanocages can be fabricated with judicious selection of the coordinating etchant, optimization of reaction conditions, and the assistance of a surfactant.

Versatility of the Strategy for Nanocage Fabrication.

This HSAB-principle-inspired and template-assisted strategy also allows rational control of the size, shell thickness, and shape of resultant MH nanocages. $\text{Ni}(\text{OH})_2$ nanomaterials are taken as an example to demonstrate this versatility as follows. Figure 6 shows the octahedral nanocages with edge lengths around

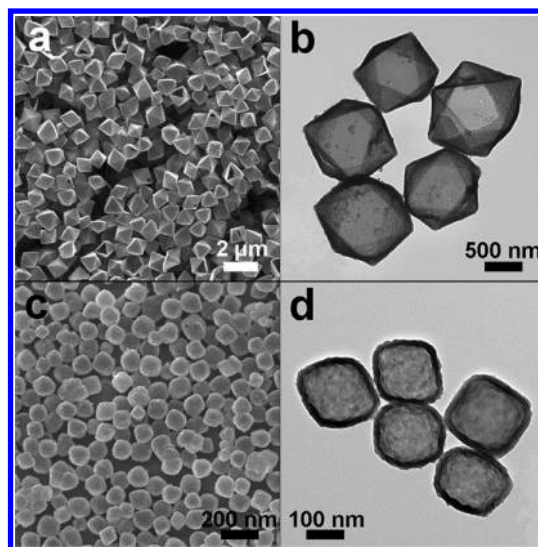


Figure 6. SEM and TEM images of the $\text{Ni}(\text{OH})_2$ nanocages with edge lengths around (a, b) 1 μm and (c, d) 170 nm.

around 1 μm and 170 nm, which can be synthesized utilizing the same procedure by taking the Cu_2O octahedra with respective sizes as the templates. Although the size range of the Cu_2O templates is wide, the reaction times are very close. This proves again the strong affinity between the etchant and the templates. In addition, the shell thickness can be controlled by changing the initial concentration of Ni^{2+} (ICN). Tuning the concentration at 0.5 and 3 times that of the typical ICN (0.7 mM) can bring about the resultant nanocages with ~ 15 and ~ 80 nm of the shell thickness, respectively (Figure 7). Thus, this provides a clue that the lower (higher) the ICN is, the thinner (thicker) the shell thickness of the nanocages would be. However, well-defined and high-quality nanocages could not be obtained by further a decrease or increase of the ICN. For instance, a much lower ICN (0.21 mM) would induce the breakage and deformation of the nanocages, while a much

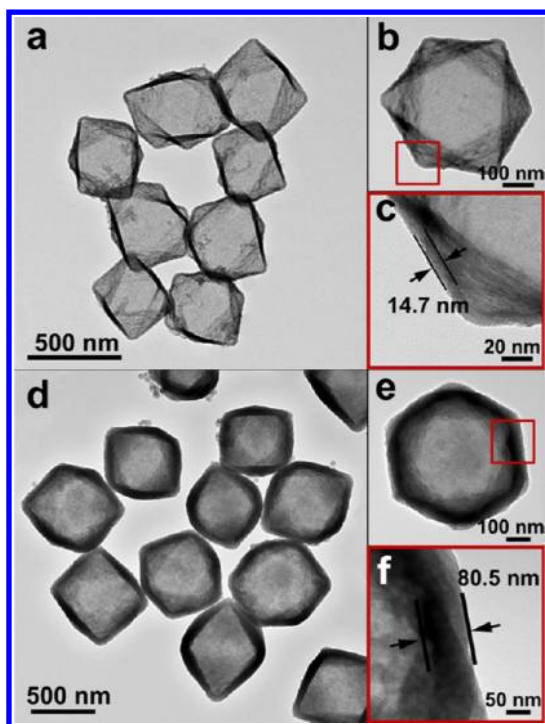


Figure 7. TEM images of the $\text{Ni}(\text{OH})_2$ nanocages with shell thickness around (a–c) 15 nm and (d–f) 80 nm. Parts c and f are the magnified images of the typical shell structure from the marked areas of the nanocages in parts b and e, respectively.

higher ICN (2.8 mM) would lead to abundant irregular $\text{Ni}(\text{OH})_2$ nanoparticles in the product (Figure S17, Supporting Information). When other morphologies of Cu_2O templates are introduced, such as cubes and spheres, the resultant $\text{Ni}(\text{OH})_2$ nanocages with corresponding shape can be also obtained, as shown in Figure 8. The features of the octahedral nanocages,

including uniform dimensions, good exterior texture, and amorphous, intact, and regular shell structure can also be clearly observed in these cubic and spherical nanocages. All these suggest that the provided strategy for the fabrication of $\text{Ni}(\text{OH})_2$ nanocages is powerful and should be suitable for preparing other kinds of MH nanocages, even templating against a more sophisticated architecture of Cu_2O .

Along with the series of MH and MO nanocages with transition-metal elements mentioned above, the provided fabricating strategy also shows potential in the synthesis of main-group-metal hydroxides and oxide nanocages. For example, uniform, amorphous, and octahedral $\text{Pb}(\text{OH})_2$ nanocages can be synthesized in a similar solution system with slight modification (Figure S18, Supporting Information). These $\text{Pb}(\text{OH})_2$ nanocages have exterior and interior structural features similar to those of the transition-metal hydroxides. Through thermal treatment at an appropriate temperature, amorphous $\text{Pb}(\text{OH})_2$ can transform to polycrystalline PbO nanocages without any structural destruction (Figure S19, Supporting Information). On the basis of these results, we believe that more interesting and important new types of nanocages can be obtained by properly tuning the chemical reactions in the fabricating process.

CONCLUSION

In summary, we have demonstrated a general strategy for the fabrication of MH and MO nanocages. A template-assisted route inspired by the HSAB principle was employed for successfully synthesizing MH nanocages via meticulous selection of the coordinating etchant as well as optimization of the reaction conditions. This unique route shows potential in designing well-defined and high-quality MH nanocages with varying components, shell thicknesses, shapes, and sizes at room temperature. Consequently, porous MO nanocages can be obtained readily just through appropriate thermal treatment

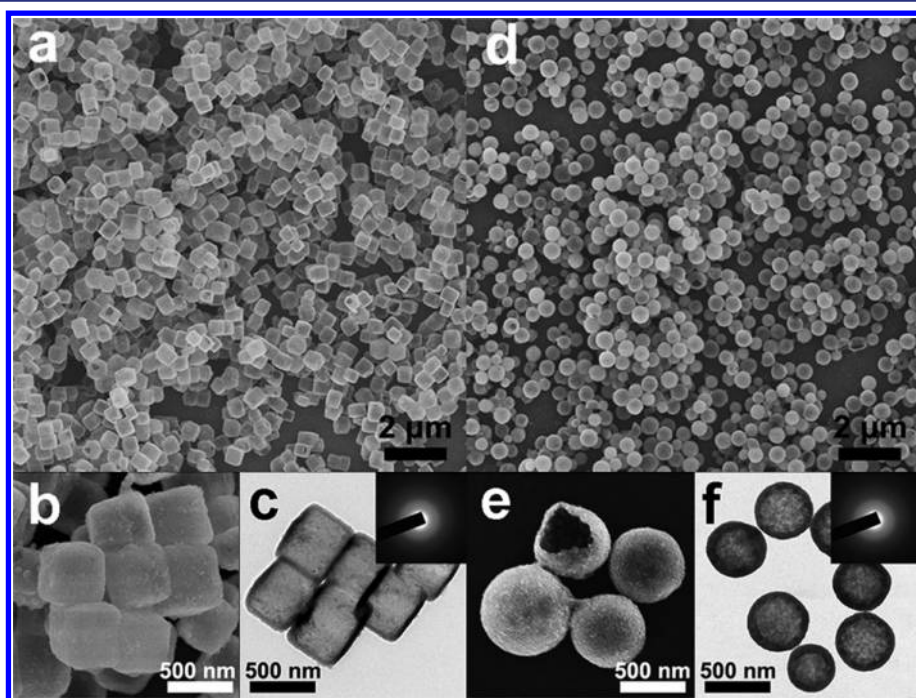


Figure 8. SEM and TEM images of $\text{Ni}(\text{OH})_2$ nanocages with (a–c) cubic and (d–f) spherical structures. The insets in parts c and f are SAED patterns, indicating the amorphous feature of the samples.

of the respective MH nanocages. The overall strategy present in this work expands the range of the application of the HSAB principle in nanoscience and offers a unique clue for rational fabrication of hollow (porous) and/or amorphous structures on the nanoscale, where these nanocages may present promising potential for various applications.

■ ASSOCIATED CONTENT

■ Supporting Information

Text, tables, and figures giving a detailed experimental section and additional material characterizations. This material is available free of charge via the Internet at <http://pubs.acs.org>.

■ AUTHOR INFORMATION

Corresponding Author

*E-mail for L.G.: guolin@buaa.edu.cn.

Notes

The authors declare no competing financial interest.

■ ACKNOWLEDGMENTS

We thank Prof. Zhiyong Tang's group at the National Center for Nanoscience and Technology of China for XPS measurements. This work was supported by the National Basic Research Program of China (No. 2010CB934700), the National Natural Science Foundation of China (51272012), and the Specialized Research Fund for the Doctoral Program of Higher Education (20111102130006).

■ REFERENCES

- (1) Sanchez, C.; Rozes, L.; Ribot, F.; Laberty-Robert, C.; Grosso, D.; Sassoie, C.; Boissiere, C.; Nicole, L. *C. R. Chim.* **2010**, *13*, 3.
- (2) Jin, R.; Charles Cao, Y.; Hao, E.; Metraux, G. S.; Schatz, G. C.; Mirkin, C. A. *Nature* **2003**, *425*, 487.
- (3) Langille, M. R.; Zhang, J.; Personick, M. L.; Li, S.; Mirkin, C. A. *Science* **2012**, *337*, 954.
- (4) Langille, M. R.; Personick, M. L.; Zhang, J.; Mirkin, C. A. *J. Am. Chem. Soc.* **2012**, *134*, 14542.
- (5) Langille, M. R.; Personick, M. L.; Zhang, J.; Mirkin, C. A. *J. Am. Chem. Soc.* **2011**, *133*, 10414.
- (6) Personick, M. L.; Langille, M. R.; Zhang, J.; Harris, N.; Schatz, G. C.; Mirkin, C. A. *J. Am. Chem. Soc.* **2011**, *133*, 6170.
- (7) Personick, M. L.; Langille, M. R.; Wu, J.; Mirkin, C. A. *J. Am. Chem. Soc.* **2013**, *135*, 3800.
- (8) Métraux, G. S.; Cao, Y. C.; Jin, R.; Mirkin, C. A. *Nano Lett.* **2003**, *3*, 519.
- (9) Wang, X.; Zhuang, J.; Peng, Q.; Li, Y. *Nature* **2005**, *437*, 121.
- (10) González, E.; Arbiol, J.; Puntes, V. F. *Science* **2011**, *334*, 1377.
- (11) Yang, J.; Sargent, E.; Kelley, S.; Ying, J. Y. *Nat. Mater.* **2009**, *8*, 683.
- (12) Zeng, Z.; Sun, T.; Zhu, J.; Huang, X.; Yin, Z.; Lu, G.; Fan, Z.; Yan, Q.; Hng, H. H.; Zhang, H. *Angew. Chem., Int. Ed.* **2012**, *51*, 9052.
- (13) Jin, Z.; Xiao, M.; Bao, Z.; Wang, P.; Wang, J. *Angew. Chem., Int. Ed.* **2012**, *51*, 6406.
- (14) Liu, H.; Qu, J.; Chen, Y.; Li, J.; Ye, F.; Lee, J. Y.; Yang, J. *J. Am. Chem. Soc.* **2012**, *134*, 11602.
- (15) Li, C. C.; Zeng, H. C. *J. Am. Chem. Soc.* **2012**, *134*, 19084.
- (16) Wang, L.; Tang, F.; Ozawa, K.; Chen, Z.-G.; Mukherj, A.; Zhu, Y.; Zou, J.; Cheng, H.-M.; Lu, G. Q. *Angew. Chem., Int. Ed.* **2009**, *48*, 7048.
- (17) Zhou, L.; Gao, C.; Hu, X.; Xu, W. *Chem. Mater.* **2011**, *23*, 1461.
- (18) Zhang, J.; Fang, J. *J. Am. Chem. Soc.* **2009**, *131*, 18543.
- (19) Ding, Y.; Gu, J.; Zhang, T.; Yin, A.-X.; Yang, L.; Zhang, Y.-W.; Yan, C.-H. *J. Am. Chem. Soc.* **2012**, *134*, 3255.
- (20) Nai, J.; Chen, Z.; Li, H.; Li, F.; Bai, Y.; Li, L.; Guo, L. *Chem. Eur. J.* **2013**, *19*, 501.
- (21) Skrabalak, S. E.; Chen, J.; Sun, Y.; Lu, X.; Au, L.; Cobley, C. M.; Xia, Y. *Acc. Chem. Res.* **2008**, *41*, 1587.
- (22) Lou, X. W.; Archer, L. A.; Yang, Z. *Adv. Mater.* **2008**, *20*, 3987.
- (23) Zhao, Y.; Jiang, L. *Adv. Mater.* **2009**, *21*, 3621.
- (24) Wang, Z.; Lou, X. W. *Adv. Mater.* **2012**, *24*, 4124.
- (25) Skrabalak, S. E.; Chen, J.; Sun, Y.; Lu, X.; Au, L.; Cobley, C. M.; Xia, Y. *Acc. Chem. Res.* **2008**, *41*, 1587.
- (26) Shchepelina, O.; Kozlovskaya, V.; Singamaneni, S.; Kharlampieva, E.; Tsukruk, V. V. *J. Mater. Chem.* **2010**, *20*, 6587.
- (27) Wang, Z.; Zhou, L.; Lou, X. W. *Adv. Mater.* **2012**, *24*, 1903.
- (28) Glotzer, S. C.; Solomon, M. J. *Nat. Mater.* **2007**, *6*, 557.
- (29) Zeng, J.; Zhang, Q.; Chen, J.; Xia, Y. *Nano Lett.* **2009**, *10*, 30.
- (30) Wang, X.; Yu, L.; Wu, X.-L.; Yuan, F.; Guo, Y.-G.; Ma, Y.; Yao, J. *J. Phys. Chem. C* **2009**, *113*, 15553.
- (31) Zhang, L.; Zhou, L.; Wu, H. B.; Xu, R.; Lou, X. W. *Angew. Chem., Int. Ed.* **2012**, *51*, 7267.
- (32) Hu, L.; Huang, Y.; Zhang, F.; Chen, Q. *Nanoscale* **2013**, *5*, 4186.
- (33) Cao, J.; Zhu, Y. C.; Bao, K. Y.; Shi, L.; Liu, S. Z.; Qian, Y. T. *J. Phys. Chem. C* **2009**, *113*, 17755.
- (34) Zeng, H. C. *J. Mater. Chem.* **2006**, *16*, 649.
- (35) Liu, B.; Zeng, H. C. *Small* **2005**, *1*, 566.
- (36) Lou, X. W.; Wang, Y.; Yuan, C.; Lee, J. Y.; Archer, L. A. *Adv. Mater.* **2006**, *18*, 2325.
- (37) Liu, B.; Zeng, H. C. *J. Am. Chem. Soc.* **2004**, *126*, 8124.
- (38) Liu, Y.; Goebel, J.; Yin, Y. *Chem. Soc. Rev.* **2013**, *42*, 2610.
- (39) Yin, Y.; Rioux, R. M.; Erdonmez, C. K.; Hughes, S.; Somorjai, G. A.; Alivisatos, A. P. *Science* **2004**, *304*, 711.
- (40) Jin fan, H.; Knez, M.; Scholz, R.; Nielsch, K.; Pippel, E.; Hesse, D.; Zacharias, M.; Gosele, U. *Nat. Mater.* **2006**, *5*, 627.
- (41) Sun, Y.; Mayers, B.; Xia, Y. *Adv. Mater.* **2003**, *15*, 641.
- (42) Wang, Z.; Luan, D.; Li, C. M.; Su, F.; Madhavi, S.; Boey, F. Y. C.; Lou, X. W. *J. Am. Chem. Soc.* **2010**, *132*, 16271.
- (43) Wang, Z.; Luan, D.; Boey, F. Y. C.; Lou, X. W. *J. Am. Chem. Soc.* **2011**, *133*, 4738.
- (44) Zhang, D.-F.; Zhang, H.; Guo, L.; Zheng, K.; Han, X.-D.; Zhang, Z. *J. Mater. Chem.* **2009**, *19*, 5220.
- (45) Shang, Y.; Zhang, D.; Guo, L. *J. Mater. Chem.* **2012**, *22*, 856.
- (46) Huang, W.-C.; Lyu, L.-M.; Yang, Y.-C.; Huang, M. H. *J. Am. Chem. Soc.* **2011**, *134*, 1261.
- (47) Ho, J.-Y.; Huang, M. H. *J. Phys. Chem. C* **2009**, *113*, 14159.
- (48) Leng, M.; Liu, M.; Zhang, Y.; Wang, Z.; Yu, C.; Yang, X.; Zhang, H.; Wang, C. *J. Am. Chem. Soc.* **2010**, *132*, 17084.
- (49) Pearson, R. G. *J. Am. Chem. Soc.* **1963**, *85*, 3533.
- (50) Nag, A.; Kovalenko, M. V.; Lee, J.-S.; Liu, W.; Spokoynny, B.; Talapin, D. V. *J. Am. Chem. Soc.* **2011**, *133*, 10612.
- (51) Sahoo, J. K.; Tahir, M. N.; Yella, A.; Schladt, T. D.; Mugnaoli, E.; Kolb, U.; Tremel, W. *Angew. Chem., Int. Ed.* **2010**, *49*, 7578.
- (52) Alyea, H. N. *J. Chem. Educ.* **1969**, *46*, A34.
- (53) Huang, M.; Tso, E.; Datye, A. K.; Prairie, M. R.; Stange, B. M. *Environ. Sci. Technol.* **1996**, *30*, 3084.
- (54) Wang, Q.; O'Hare, D. *Chem. Rev.* **2012**, *112*, 4124.
- (55) Jun, Y.-w.; Choi, J.-s.; Cheon, J. *Angew. Chem., Int. Ed.* **2006**, *45*, 3414.
- (56) Jiang, J.; Li, Y.; Liu, J.; Huang, X.; Yuan, C.; Lou, X. W. *Adv. Mater.* **2012**, *24*, 5166.
- (57) Patzke, G. R.; Zhou, Y.; Kontic, R.; Conrad, F. *Angew. Chem., Int. Ed.* **2011**, *50*, 826.
- (58) Biesinger, M. C.; Payne, B. P.; Grosvenor, A. P.; Lau, L. W. M.; Gerson, A. R.; Smart, R. S. C. *Appl. Surf. Sci.* **2011**, *257*, 2717.
- (59) Peck, M. A.; Langell, M. A. *Chem. Mater.* **2012**, *24*, 4483.
- (60) Dupin, J.-C.; Gonbeau, D.; Vinatier, P.; Levasseur, A. *Phys. Chem. Phys.* **2000**, *2*, 1319.
- (61) Biesinger, M. C.; Lau, L. W. M.; Gerson, A. R.; Smart, R. S. C. *Appl. Surf. Sci.* **2010**, *257*, 887.
- (62) Rich, L. R. *Inorganic Reactions in Water*; Springer-Verlag: Berlin, Heidelberg, 2007; Section 16.
- (63) Li, H. B.; Yu, M. H.; Wang, F. X.; Liu, P.; Liang, Y.; Xiao, J.; Wang, C. X.; Tong, Y. X.; Yang, G. W. *Nat. Commun.* **2013**, *4*, 1894.

- (64) Guo, J.; Liu, Q.; Wang, C.; Zachariah, M. R. *Adv. Funct. Mater.* **2012**, *22*, 803.
- (65) Hall, J. W.; Membreno, N.; Wu, J.; Celio, H.; Jones, R. A.; Stevenson, K. J. *J. Am. Chem. Soc.* **2012**, *134*, 5532.
- (66) Wang, X.-L.; Han, W.-Q.; Chen, H.; Bai, J.; Tyson, T. A.; Yu, X.-Q.; Wang, X.-J.; Yang, X.-Q. *J. Am. Chem. Soc.* **2011**, *133*, 20692.
- (67) Li, Y.; Sasaki, T.; Shimizu, Y.; Koshizaki, N. *J. Am. Chem. Soc.* **2008**, *130*, 14755.
- (68) Choi, S.-H.; Hwang, D.; Kim, D.-Y.; Kervella, Y.; Maldivi, P.; Jang, S.-Y.; Demadrille, R.; Kim, I.-D. *Adv. Funct. Mater.* **2013**, DOI: 10.1002/adfm.201203278.
- (69) Shang, C.; Dong, S.; Wang, S.; Xiao, D.; Han, P.; Wang, X.; Gu, L.; Cui, G. *ACS Nano* **2013**, DOI: 10.1002/nn401402a.
- (70) Tao, Y.; Zaijun, L.; Ruiyi, L.; Qi, N.; Hui, K.; Yulian, N.; Junkang, L. *J. Mater. Chem.* **2012**, *22*, 23587.
- (71) Li, Y.; Fu, Z.-Y.; Su, B.-L. *Adv. Funct. Mater.* **2012**, *22*, 4634.
- (72) Zhang, J.; Li, C. M. *Chem. Soc. Rev.* **2012**, *41*, 7016.
- (73) Xiong, S.; Zeng, H. C. *Angew. Chem., Int. Ed.* **2012**, *51*, 949.